Title

Real-time mapping of photo-sono therapy induced cavitation using Doppler optical coherence tomography.

Journal

Optics Letters, 49(17)

ISSN

0146-9592

Authors

Song, Yuchen
Wei, Shuang
Li, Yan
et al.

Publication Date

2024-09-01

DOI

10.1364/ol.532993

Optics Letters

Real-time mapping of photo-sono therapy induced cavitation using Doppler optical coherence tomography

Yuchen Song,[1,2] Shuang Wei,[1,2] Yan Li,[1,2] Fengyi Zhang,[1,2] Zhikai Zhu,[1,2] Lidek Chou,[1,2] Wancun Jia,[1,2] Runze Li,[3] Qifa Zhou,[3] and Zhongping Chen[1,2,*]

[1]Beckman Laser Institute, University of California Irvine, Irvine, California 92612, USA
[2]Department of Biomedical Engineering, University of California Irvine, Irvine, California 92612, USA
[3]Department of Biomedical Engineering, University of Southern California, Los Angeles, California 90089, USA
*z2chen@uci.edu

Received 24 June 2024; revised 27 July 2024; accepted 28 July 2024; posted 2 August 2024; published 21 August 2024

Photo-sono therapy (PST) is an innovative anti-vascular approach based on cavitation-induced spallation. Currently, passive cavitation detection (PCD) is the prevalent technique for cavitation monitoring during treatment. However, the limitations of PCD are the lack of spatial information of bubbles and the difficulty of integration with the PST system. To address this, we proposed a new, to the best of our knowledge, cavitation mapping method that integrates Doppler optical coherence tomography (OCT) with PST to visualize bubble dynamics in real time. The feasibility of the proposed system has been confirmed through experiments on vascular-mimicking phantoms and in vivo rabbit ear vessels, and the results are compared to high-speed camera observations and PCD data. The findings demonstrate that Doppler OCT effectively maps cavitation in real time and holds promise for guiding PST treatments and other cavitation-related clinical applications.

https://doi.org/10.1364/OL.532993

Cavitation plays an important role in therapeutic purposes such as thrombolysis [1], drug delivery [2,3], tissue ablation [4], therapeutic angiogenesis [5], and vascular occlusion therapy [6]. As a new cavitation based anti-vascular technique, photo-sono therapy (PST) applies nanosecond laser pulses and ultrasound (US) bursts simultaneously to promote a cavitation activity to destruct blood vessels [7,–,9]. Compared to conventional ultrasonic cavitation methods, PST is highly selective and provides precisely localized treatment. This is because cavitation is limited to the blood vessels due to the fact that hemoglobin, the major chromophore in blood, absorbs light more effectively at the working wavelength as compared to surrounding tissues [10]. This technique has been explored for the treatment of various diseases, including diabetic retinopathy, age-related macular degeneration, and port-wine stains [11–13]. However, due to the variability in biological responses, both over-treatment and under-treatment can occur during PST [14]. Therefore, real-time monitoring of treatment responses is essential to enhance the safety and efficacy of PST.

As PST is a cavitation-based method, observing both the structure of microvessels and the spatiotemporal distribution of cavitation bubbles is essential for optimizing the therapeutic process. Several noninvasive techniques have been employed to visualize vasculature changes during PST treatment, including ultrasound imaging [8], photoacoustic imaging [15], and optical coherence tomography [9]. Furthermore, various optical and acoustic methods have been utilized for detecting bubble dynamics, including high-speed photography [16], active cavitation detection (ACD) [17], and passive cavitation detection [18]. However, conventional photography is limited to transparent media and only captures two-dimensional projections of three-dimensional scenes. Traditional ACD and PCD methods typically use a single-element ultrasound transducer, which cannot differentiate signals from multiple source locations, therefore providing poor spatial resolution. Although an ultrasound array can be used to map bubble dynamics in 2D/3D, it requires an extra transducer array that increases the complexity and cost of the overall system [19,20]. Therefore, having a modality capable of discerning both spatiotemporal bubble dynamics and microvessels is crucial for an effective personalized PST treatment.

OCT is a promising tool for assessing tissue morphology, providing histopathological information both before and during treatment. Compared to ultrasound imaging, OCT offers higher resolution and accuracy, and compared to photoacoustic imaging, it provides detailed layered structures of the skin tissue. Moreover, functional OCT imaging, including Doppler OCT and OCT angiography, extends OCT capabilities to assess blood flow and high-resolution microvasculature [21–25]. These advanced imaging techniques have been utilized for pre-treatment assessment and monitoring during laser therapy [26]. However, bubble dynamics during PST have not yet been detectable using an OCT system. The presence of bubble clusters can affect the backscattered signal, and the collapse of bubbles generates circumferential and shear stress, influencing blood flow velocity [27]. A recent study reported that PST-induced cavitation causes

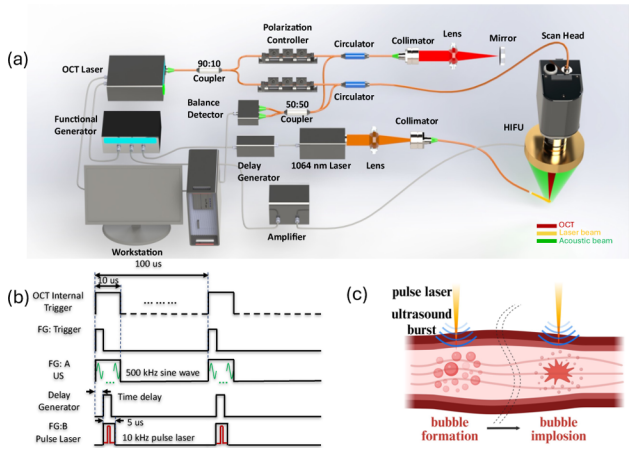

Fig. 1. Design and principle of the Doppler OCT-guided PST system. (a) Schematic of the Doppler OCT-guided PST system. (b) Timing diagram. FG, function generator, US, ultrasound. (c) Principle of PST-induced cavitation.

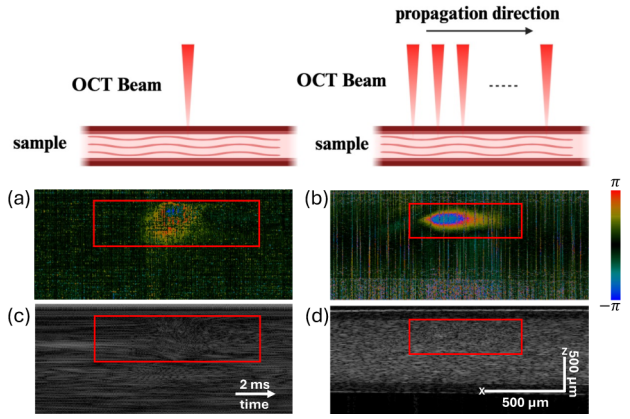

Fig. 2. Cavitation observation with SS-OCT in phantom. (a) Doppler OCT image, (b) Doppler OCT image, (c) conventional OCT image under M-mode acquisition, as a function of time, (d) conventional OCT image under B-mode acquisition, as a function of space.

washout in OCT-detected signal [28]. However, traditional OCT detection cannot quantitatively analyze bubble dynamics or the interaction with surrounding tissues. Here, we propose a method to detect bubble dynamics in real time by observing blood flow changes caused by bubble implosion. This method integrates high sensitivity of phase-resolved Doppler OCT with conventional OCT to detect both tissue morphology and cavitation within the same system, without the need for additional cavitation detection components.

In this Letter, we demonstrate that Doppler OCT can provide real-time mapping of the distribution of cavitation in both vascular-mimicking phantoms and rabbit ears during PST. A phase-resolved Doppler OCT system was developed to detect blood flow velocity changes induced by the cavitation process. To validate the performance of this system, we compared the results from Doppler OCT with those obtained from a PCD and high-speed camera. Doppler OCT can detect cavitation induced under various laser energy and ultrasound pressure settings, providing a valuable tool for guiding PST treatment.

The system comprises two main components: Doppler OCT and PST, as illustrated in Fig. 1(a). In the Doppler OCT subsystem, a micro-electro-mechanical (MEMS)-tunable vertical cavity surface emitting laser (VCSEL) swept source (SS) is utilized, featuring a sweep rate of 100 kHz and a bandwidth of 100 nm (SL1310V1, Thorlabs, NJ, USA). The balanced detector operates in the 1200–1700 nm wavelength range and has a 1.6 GHz bandwidth (PDB480C-AC, Thorlabs, NJ, USA). The sensitivity, axial resolution, and lateral resolution of our SS-OCT system are approximately 110 dB, 9 μm, and 30 μm, respectively. For the PST subsystem, a 0.5 MHz high-intensity focused ultrasound (HIFU) transducer with a focal width of 3.02 mm and a focal length of 21.42 mm (H-107, Sonic Concepts, WA, USA) is employed. The nanosecond pulsed laser operates at a wavelength of 1064 nm, with a 10 kHz repetition rate and a 10 ns pulse duration (SOL-1064, Bright Solutions, Italy). A pulse/delay generator is used to synchronize pulsed laser emission and ultrasound generation. The ultrasound transducer is driven by a 50 dB power amplifier (3100L, Electronics & Innovation, NY, USA). The time delay between a laser pulse and an ultrasound pulse is measured using an oscilloscope to monitor the output of a pulser/receiver. Figure 1(b) provides a detailed timing diagram for the Doppler OCT-guided PST system. The trigger for both the pulsed laser and ultrasound originates from the 100 kHz VCSEL but is downsampled to 10 kHz, with each trigger cycle generating five ultrasound bursts and one laser pulse. The principle of the Doppler OCT-guided PST system is shown in Fig. 1(c). Inertial cavitation is induced by both an ultrasound burst and a laser pulse; meanwhile, the circumferential and shear stress generated by bubble implosions cause changes in blood flow velocity, which is detected by phase-resolved Doppler OCT. The relationship between velocity V and phase change $\Delta\phi$ can be determined by the following equation [29,30]:

$$V = \frac{\Delta\phi * \lambda_0}{4\pi * n * \Delta T * \cos\theta} \quad (1)$$

where $\Delta\phi$ is the phase change between adjacent A-lines, ΔT is the time interval between A-lines, λ_0 is the center wavelength of the swept source laser, n is the refractive index, and θ is the angle between the incident beam and blood flow. The phase change can be measured from adjacent A-line based on a cross-correlation algorithm:

$$\Delta\phi_{i,j} = \tan^{-1}\left[\frac{\mathrm{Im}(F_{j,i} * F_{j+1,i})}{\mathrm{Re}(F_{j,i} * F_{j+1,i})}\right] \quad (2)$$

where $F_{j,i}$ is the OCT complex signal at j_{th} A-line, i_{th} depth and $F_{j+1,i}$ is the OCT complex signal at $(j+1)_{th}$ A-line, i_{th} depth.

The first experiment aims to demonstrate the performance of Doppler OCT in monitoring cavitation during PST. Here, porcine blood is perfused into a polytetrafluoroethylene (PTFE) tube (inner diameter, 1.2 mm; outer diameter, 1.5 mm, Zeus Inc.) to mimic human vessels. The bubble dynamics is captured by a stationary OCT beam (M-mode) and a scanning beam (B-mode) for temporal and spatial information, respectively. The region depicting the spatiotemporal distribution of bubble dynamics is marked with a red box in each subfigure in Fig. 2. The temporal properties of bubble dynamics under M-mode imaging using Doppler OCT and traditional OCT are shown in Figs. 2(a) and 2(c), respectively. Each frame consists of 1000 A-lines, with the effect of bubble cluster implosions lasting approximately 2 ms. The spatial information regarding cavitation-induced velocity changes can be observed in

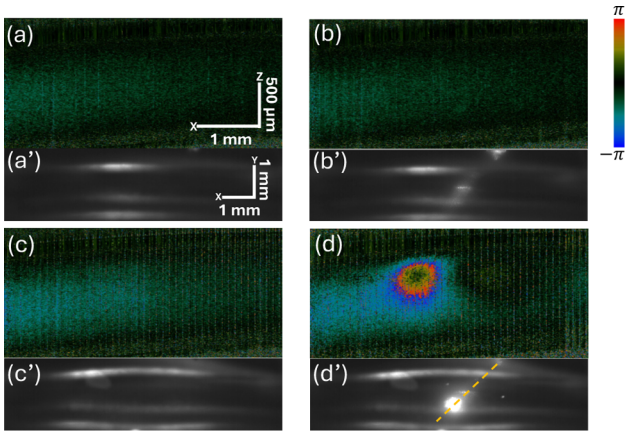

Fig. 3. Cavitation detection in flow blood phantom. Color images and black-and-white images are captured by Doppler OCT (a)–(d) and high-speed camera (a')–(d'), respectively. (a) Control group: without pulsed laser and without US, (b) pulsed laser only at 2.76 mJ/cm^2, (c) ultrasound only at 310 kPa, (d) with both pulsed laser and with US.

B-mode images, as illustrated in Figs. 2(b) and 2(d). Each frame also contains 1000 A-lines, with the cavitation-induced stress covering approximately 500 μm. Although conventional OCT can detect speckle variations induced by cavitation, the results lack the quantitative measurement of implosion-induced deformation compared to those delivered by Doppler OCT images. Phase wrap results are observed in Doppler results, because of the phase change over the detection range. Based on Eq. (1), the unwrap detected velocity inter A-line is around $[-3.275, 3.275]$ cm/s.

To verify whether bubble implosion occurs only during PST, we utilized both Doppler OCT and a high-speed camera (HotShot 1280 INT, NAC Americas, Inc., MA, USA) to monitor the cavitation events. The frame rates of the Doppler OCT and high-speed camera are 100 Hz and 3000 Hz, respectively. The phantom setup was exposed to laser alone (at 2.76 mJ/cm^2), ultrasound alone (at 310 kPa), and both laser and ultrasound, as depicted in Fig. 3. The blood in the vascular-mimicking phantom was driven using a syringe pump at a speed of 1 cm/s. The phase change measured by Doppler OCT was consistent with the predetermined blood flow without any external influence, as seen in Fig. 3(a). Low-energy laser pulses alone do not affect blood flow in the Doppler OCT images [Fig. 3(b)]; however, the pulsed laser beam and its focal spot can be observed using the high-speed camera [Fig. 3(b')]. Low-pressure ultrasound bursts alone cause periodic noise that appears as stripes in the Doppler OCT image [Fig. 3(c)], corresponding to the 10 kHz trigger for driving the HIFU transducer. In addition, the slight expansion of the vascular phantom can be observed with the camera [Fig. 3(c')]. Blood velocity changes are observed only when both the ultrasound and pulsed laser were applied simultaneously. Both Doppler OCT and the high-speed camera detected bubble dynamics induced by PST in a millimeter-scale region. The difference lies in the detection methods: Doppler OCT measures blood velocity changes in a cross section [Fig. 3(d)], whereas the high-speed camera captures variations in the reflected light in a 2D projection [Fig. 3(d')].

To demonstrate the feasibility of the integrated system *in vivo*, three male New Zealand white rabbits were used, and

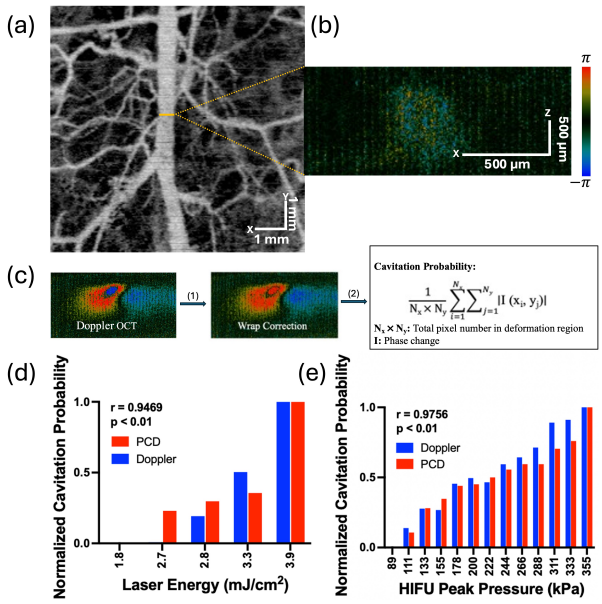

Fig. 4. Cavitation detection during PST in a rabbit ear *in vivo*. (a) OCTA image captured before PST. (b) Bubble dynamics at a selected location [indicated by the yellow line in Fig. 4(a)] during PST. (c) Algorithm for estimating cavitation probability based on Doppler OCT images, consisting of (1) phase wrap correction and (2) cavitation probability estimation. Correlation between normalized power detected by PCD and normalized cavitation probability detected by Doppler OCT with varying laser energy (d) and HIFU peak pressure (e).

10 sites on each rabbit were imaged. Figure 4(a) presents a representative OCT angiography (OCTA) image from a rabbit's ear, and Fig. 4(b) shows the Doppler OCT image depicting bubble dynamics during PST (laser energy, 3.3 mJ/cm^2, and HIFU peak pressure, 288.4 kPa) at a selected location. To quantitatively estimate the cavitation probability, the phase wrap induced by strong bubble implosion is corrected, followed by calculating the average phase change in the deformation region to reflect the stress induced by bubble collapse, as shown in Fig. 4(c). Subsequently, PCD was employed to estimate the cavitation effect and compared to Doppler OCT results. The detection transducer had a center frequency of 15 MHz, and the detection frequency range is from 11 MHz to 19 MHz. Laser energy was gradually increased from 1.77 mJ/cm^2 to 3.88 mJ/cm^2 and the HIFU peak pressure from 88.74 kPa to 354.96 kPa. To estimate the cavitation activity detected by PCD, acoustic signal is analyzed in the frequency domain, removing spectrum components below 0.5 MHz. The remaining components are integrated to represent cavitation probability. For Doppler OCT results, the sum of the absolute values of phase changes within deformation regions is integrated to indicate cavitation probability. The cavitation probabilities for both PCD and Doppler OCT are normalized according to different parameter settings. The phase change in Doppler OCT images and the integration of normalized power spectra of PCD detected signals revealed a strong positive correlation ($r = 0.9756$ and $r = 0.9469$, respectively), as seen in Figs. 4(d) and 4(e). These results demonstrate that the phase changes observed from OCT B-scan images highly correlate with the power spectra from PCD, suggesting that Doppler OCT

can serve as an alternative method for monitoring cavitation events.

In summary, we developed a Doppler OCT-guided PST system to map cavitation in real time. This method enables monitoring of both microvascular morphology and cavitation events using a single system. The validity of Doppler OCT results has been corroborated with a conventional high-speed camera and PCD methods. Compared to these methods, Doppler OCT provides both spatial and temporal information on cavitation and offers a quantitative approach to evaluate bubble dynamic-induced deformations. However, it should be noted that Doppler OCT is effective for inertial cavitation, as bubble implosion induces deformation within the medium. However, under low laser and ultrasound parameter settings, stable cavitation predominates during treatment. Doppler OCT shows no detection, while PCD detects harmonic signals. The detection range of Doppler OCT can be further enhanced by calculating the phase difference over a larger time interval by skipping several A-lines. Moreover, the current experimental design is limited in imaging speed, which is the reason why Doppler results have a phase wrap and make it challenging for 3D imaging. Recently, MHz swept-source lasers have been used for volumetric imaging, making it possible for 3D cavitation detection with Doppler OCT [31]. Additionally, velocity changes can only be detected along the direction of the OCT beam path; therefore, they cannot represent the true distribution of cavitation-induced stress. The future work will focus on increasing the imaging speed with faster swept laser sources and incorporating multiple incident beam angles to facilitate 3D detection and reconstruction of bubble dynamics during PST treatment. This method has potential applications in guiding and optimizing PST treatments and other cavitation-related clinical applications.

Funding. National Institute of Health (R01EB-030024, R01EB-030558, R01HL-125084); Air Force Office of Scientific Research (FA9550-23-1-0685).

Disclosures. The authors declare no conflicts of interest.

Data availability. Data underlying the results presented in this paper are not publicly available at this time but may be obtained from the authors upon reasonable request.

REFERENCES

1. S. Pfaffenberger, B. Devcic-Kuhar, S. P. Kastl, *et al.*, Thromb. Haemostasis **94**, 26 (2005).
2. W. G. Pitt, G. A. Husseini, and B. J. Staples, Expert Opin. Drug Delivery **1**, 37 (2004).
3. S. Roovers, T. Segers, G. Lajoinie, *et al.*, Langmuir **35**, 10173 (2019).
4. W. W. Roberts, T. L. Hall, K. Ives, *et al.*, J. Urology **175**, 734 (2006).
5. S. Young and M. Dyson, Ultrasound in Medicine & Biology **16**, 261 (1990).
6. K. Hynynen, V. Colucci, A. Chung, *et al.*, Ultrasound in Medicine & Biology **22**, 1071 (1996).
7. H. Cui, T. Zhang, and X. Yang, Appl. Phys. Lett. **102**, 133702 (2013).
8. Z. Hu, H. Zhang, A. Mordovanakis, *et al.*, Sci. Rep. **7**, 40243 (2017).
9. Y. Li, Y. Song, R. Li, *et al.*, Sci. Rep. **12**, 19916 (2022).
10. M. Wang, R. Singh, W. Zhang, *et al.*, JID Innovations **3**, 100237 (2023).
11. R. Singh, J. Jo, M. Riegel, *et al.*, Med. Phys. **48**, 4128 (2021).
12. M. Wang, Y. Qin, T. Wang, *et al.*, Lasers Surg. Med. **52**, 984 (2020).
13. Y. Qin, Y. Yu, J. Fu, *et al.*, Lasers Surg. Med. **54**, 747 (2022).
14. M. I. van Raath, S. Chohan, A. Wolkerstorfer, *et al.*, J. European Academy of Dermatology and Venereology **33**, 1369 (2019).
15. W. Zhang, Y. Qin, X. Xie, *et al.*, Opt. Lett. **44**, 4063 (2019).
16. H. Chen, W. Kreider, A. A. Brayman, *et al.*, Phys. Rev. Lett. **106**, 034301 (2011).
17. R. A. Roy, S. I. Madanshetty, and R. E. Apfel, J. Acoust. Soc. Am. **87**, 2451 (1990).
18. J. Frohly, S. Labouret, C. Bruneel, *et al.*, J. Acoust. Soc. Am. **108**, 2012 (2000).
19. M. Li, J. Gu, T. Vu, *et al.*, IEEE Trans. Ultrason., Ferroelect., Freq. Contr. **68**, 2361 (2021).
20. M. Gyöngy and C.-C. Coussios, J. Acoust. Soc. Am. **128**, EL175 (2010).
21. J. S. Nelson, K. M. Kelly, Y. Zhao, *et al.*, Arch. Dermatol. **137**, 741 (2001).
22. Z. Chen, T. E. Milner, S. Srinivas, *et al.*, Opt. Lett. **22**, 1119 (1997).
23. Z. Chen, T. E. Milner, D. Dave, *et al.*, Opt. Lett. **22**, 64 (1997).
24. Y. Zhao, K. M. Brecke, H. Ren, *et al.*, IEEE J. Sel. Top. Quantum Electron. **7**, 931 (2001).
25. Y. Li, R. S. Murthy, Y. Zhu, *et al.*, IEEE Trans. Med. Imaging **40**, 2507 (2021).
26. E. V. Gubarkova, F. I. Feldchtein, E. V. Zagaynova, *et al.*, Sci. Rep. **9**, 18670 (2019).
27. R. Singh and X. Yang, AIP Adv. **12**, 045020 (2022).
28. M. Wang, W. Zhang, Z. Chen, *et al.*, IEEE Trans. Biomed. Eng. **71**, 2473 (2024).
29. Y. Zhao, Z. Chen, C. Saxer, *et al.*, Opt. Lett. **25**, 114 (2000).
30. Y. Zhao, Z. Chen, C. Saxer, *et al.*, Opt. Lett. **25**, 1358 (2000).
31. A. Britten, P. Matten, J. Weiss, *et al.*, Biomed. Opt. Express **14**, 846 (2023).